Preprint Manuscript: Bridgelall, R. (2022). Characterizing Ride Quality with a Composite Roughness Index. *Transactions on Intelligent Transportation Systems*, DOI: 10.1109/TITS.2021.3140177.

Characterizing Ride Quality with a Composite Roughness Index

Raj Bridgelall, *Senior Member, IEEE*

***Abstract*—There are many important applications that require ride quality characterization. However, the only international standard that specifies a roughness index is not suitable for applications beyond assessing the ride quality of paved roads. Other potential applications include automated ride quality characterization of gravel roads, bike or wheelchair paths, railways, rivers, airways, hyperloops, and elevator channels. This work proposes a composite index that characterizes roughness from multidimensional movements along any path. Statistical tests demonstrate two important properties—that the index is consistent based on an ever-decreasing margin-of-error of the mean, and distinguishable among different paths. A low-cost sensor package of accelerometers, gyroscopes, and a speedometer produced the data for spatio-temporal transformation. The experiments conducted on buses revealed that both the consistency and distinguishability of the index improves with the number of measurements. The approach is best suited for applications that can use in-situ sensors or crowdsensing to automate ride quality characterization.**

***Index Terms*—international roughness index, ride comfort, maintenance decision support system, probe vehicle, vehicle design**

I. Introduction

Transportation agencies use the International Roughness Index (IRI) to characterize pavement roughness for maintenance planning and construction quality assurance. The IRI is the most common measure of ride quality used worldwide [1]. Even so, IRI specifications vary widely, even across jurisdictions of the same country [2]. In general, the IRI characterizes pavement roughness based on variations in the longitudinal profile [3]. However, many other aspects of roadway geometry such as curvature and transversal slope affect the roughness that riders perceive [4].

Some other important applications that require ride quality characterization include autonomous vehicle control [5], high-speed elevator operation [6], high-speed rail or hyperloop operation [7], passenger transit driver training [8], vibration impacts on ambulance patients [9], construction equipment safety [10], vibration impacts on sensitive cargo [11], wheelchair safety [12], pedestrian walkway safety [13], classification of car driving safety [14], and insurance pricing based on driving behavior [15].

The transportation literature usually associates road roughness or ride quality with vertical accelerations. Currently, there are no ride quality indices that account for the roughness perceived from all linear and rotational motions. Hence, the **contribution** of this research is a composite roughness index (CRI) that characterizes roughness from all possible motions of an object moving along any path at varying speeds. The associated **objectives** of this research are to develop a single roughness index that:

1) characterizes roughness felt from motions in all spatial dimensions,
2) is *consistent* for a given traversal path, and
3) is *distinguishable* among different traversal paths.

It is important to highlight that the CRI represents roughness in all spatial dimensions, not just vertically as the IRI does. The research methods characterize *consistency* as the amount of central tendency in the distribution of the CRIs whereas *distinguishability* is the ability of common statistical methods to distinguish among the means of those distributions.

Section 2 reviews the literature on methods to characterize roughness and related works. Section 3 details the development of the CRI, including the data collection, feature extraction, and statistical tests for consistency and distinguishability. Section 4 parallels the subsections of the methods section to visualize the results. Section 5 discusses the results, significance of the statistical tests, applicability of the index, and limitations of the work. Section 6 concludes the study and hints at future work.

II. Literature Review

This section highlights existing indices and techniques used to characterize roughness, their dominant applications, and their limitations relative to the proposed data driven approach of this work. Múčka (2016) evaluated 14 newer alternative indices to the IRI and found that most are actually based on the IRI, thus inhereting the IRI limitations [16]. For example, Gillespie and Karamihas (2000) suggested a variant of the IRI to analyze truck dynamic wheel loads [17]. Similarly, Nguyen et al. (2021) proposed a ride quality index for buses that modified parameters of the quarter-car simulation model used to produce the IRI [18]. Piryonesi & El-Diraby (2021) compared the IRI with the second most popular indicator of pavement roughness, the Pavement Condition Index (PCI), and found that the relationships vary depending on location, road type, and slope [19]. Alhasan et al. (2016) combined the IRI-based quarter-car simulations with wavelet analysis to provide a spatial assessment of roughness based on frequency bands [20]. Múčka (2020) determined a relationship between the vibration dose value (VDV) in passenger cars as a function of the IRI by measuring accelerations along three orthogonal axes and two point locations [21]. In related work, Obrien et al. (2006) proposed a roughness index to characterize bridge dynamics based on a linear combination of changes in deck surface profile [22].

Another widely used measure of roughness is based on the ISO 2631 standard that specifies vibration safety [23]. Unlike the IRI, the ISO 2631 standard combines the power spectral density of linear accelerations in each spatial dimension by using a weighted root-mean-square (RMS) of each component. However, the RMS calculation does not localize roughness like the IRI does by specifying a spatial distance window parameter along the traversal path. The EN 12299 standard developed to evaluate the influence of dynamic effects on the comfort of train passengers uses the ISO 2631 method with some modifications to the RMS weights [24]. Maternini & Cadei (2014) modified the EN 12299 method for buses and found that comfort level dropped in roundabouts because of increased transversal accelerations [25]. Barabino et al. (2019) used the ISO 2631 method to develop a new scale for evaluating the real-time driving style of bus transit services [26]. Similarly, Loprencipe et al. (2021) used the ISO 2631 standard to assess pavement decay levels based on measurements from an inertial measurement unit [27]. In related work, Wåhlberg (2006) discovered that passengers experienced more uncomfortable rides after drivers underwent training to operate buses in a more fuel-efficient manner [8].

More recent developments focused on using smartphones to collect pavement condition data to guide optimum maintenance strategies [28]. Consequently, numerous smartphone applications to characterize ride quality, including several commercial products, are now available for evaluation [29]. Partridge et al. (2021) used smartphones to measure vertical accelerations from road surface irregularities and microphones to measure engine noise to assess the potential harm of vibration and audio noise to sick premature infants during ambulance transfer between hospitals [9]. Yang, et al. (2020) cautioned that one important limitation of using smartphones for individual roughness measurements is the sensitivity variations among devices and models [30]. Nevertheless, others demonstrated that smartphones can be a useful tool to evaluate driver behavior [31].

Crowdsourced sensing or crowdsensing recently emerged to leverage the larger data volume from connected vehicles or in-vehicle smartphones. Medina, et al. (2020) found that a larger volume of measurements from a crowdsourced approach can reduce statistical variations from different devices [32]. Similarly, Zhao et al. (2016) applied the ISO 2631 method to measurements aggregated from crowdsourced smartphone data to evaluate bus ride comfort and found that both signal filtering and spatial transformation was necessary to provide consistent results [33]. Chuang et al. (2019) found that using crowdsourced data of vertical and lateral accelerations to detect roadway anomalies resulted in a 98% accuracy and a false positive rate of 1.3% [34].

Overall, there has been little effort beyond variants of the existing IRI, ISO, and EN standards to develop a data driven roughness index that is suitable of many other applications. In fact, a recent review found that, even for paved roads, a data driven method to measure roughness is still lacking [35]. None of the proposed measures of roughness included the dynamic effects from forces induced by rotations, which can be more pronounced than linear forces in vehicles like excavation equipment that rotate rapidly without moving from a spot. Hence, this work will help to close those research gaps.

III. Methods

The next three subsections describe the data collection setup, the data format, and the selected method of feature extraction. Subsequently, the four subsections that follow define the CRI, methods to evaluate interactions among the measurement dimensions, methods to assess the consistency of the CRIs, and a method to assess the distinguishability of CRIs among different traversal paths. Fig. 1 summarizes the workflow to generate the CRIs. The figure indicates a data cleaning procedure that assured data consistency from every sensor. For example, the procedure removed sensor streams with GPS

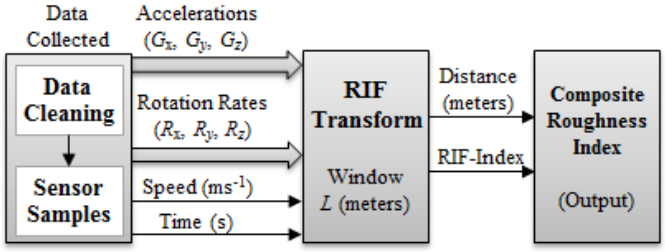

Fig. 1. Workflow to generate the CRIs.

outliers, missing coordinates, and any large gaps in accelerometer samples. The cleaning procedure then fed the cleaned data (indicated by the arrow) into another procedure that combined the sensor samples into a format required for the mathematical transformation to produce the CRIs.

A. Data Collection

The laws of Newtonian mechanics dictate that linear accelerations along any of the three spatial dimensions (x, y, z) create independent linear forces of magnitude

$$f_l = ma \tag{1}$$

where a is acceleration in m·s^{-2} and m is the mass in kilograms upon which the force is acting [36]. Rotations around each axis of the three spatial dimensions create independent centrifugal forces of magnitude

$$f_c = mr\omega^2 \tag{2}$$

where m is the mass located at a radial distance r from the axis of a plane that is rotating at a rate of ω radians-per-second about that axis. Hence, linear accelerations in the lateral, longitudinal, and vertical directions create three independent linear forces whereas rotations around those three directions create three more independent forces. Therefore, movements can create six independent forces that manifest as roughness when the forces change in time.

Capturing roughness from changes in the six forces requires measuring linear accelerations in each spatial dimension as well as measuring rotation rates about each spatial axis. Hence, the experiments used three accelerometers and three gyroscopes. The required data also included vehicle speed and the time instants of each sample. All experiments used the same smartphone (iPhone® 6s) and setup for consistency. The

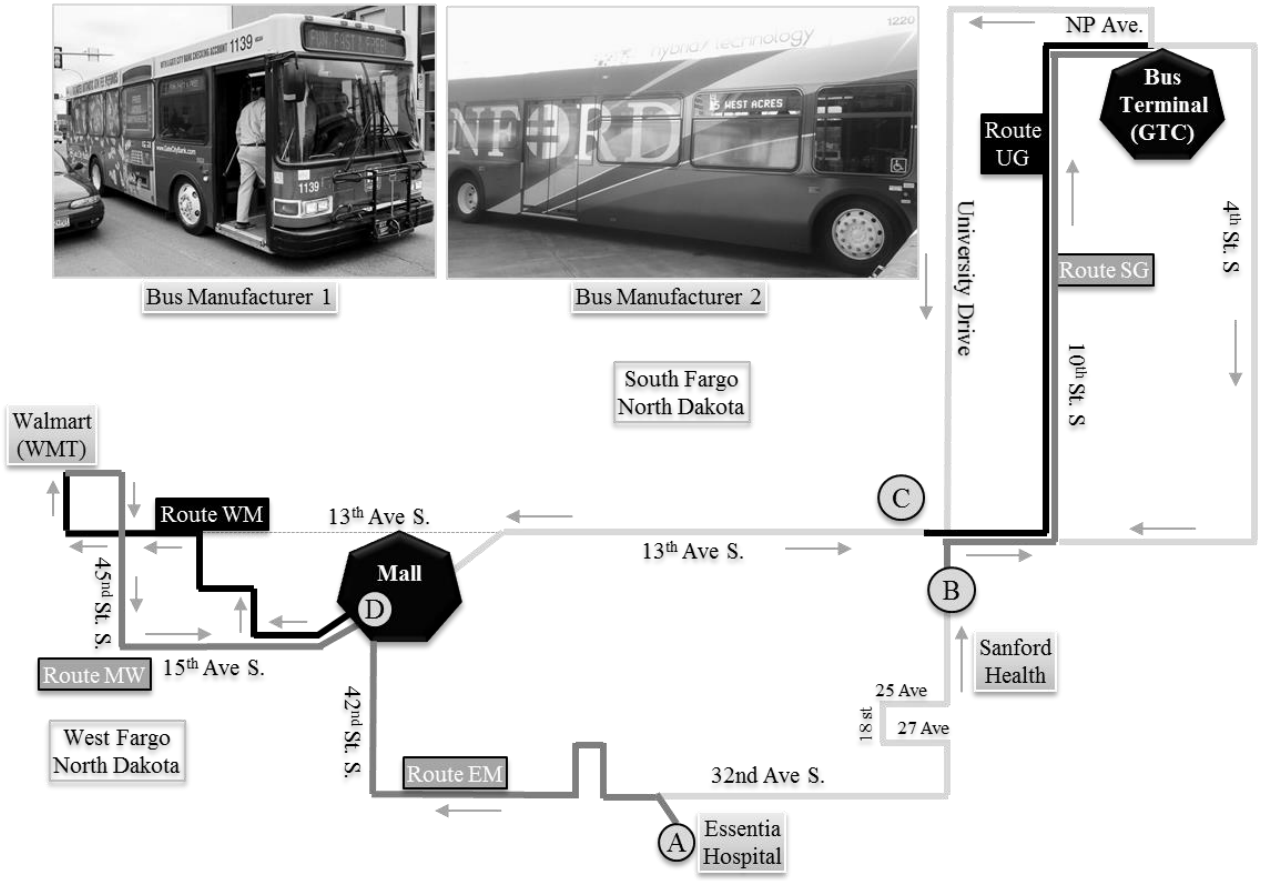

Fig. 2. Route map for data collection.

smartphone included all the sensors and functionality needed. A custom software application on the smartphone synchronized the data sampling and data logging from each sensor and formatted the merged data for post processing.

The vehicles used to collect the data were 18 different buses that serviced five routes in the small urban city of Fargo, North Dakota, U.S.A. The buses were primarily from two different manufacturers as pictured in the inset of Fig. 2. The vehicle mix was comprised of several different model years from each manufacturer. For consistency, the data collection occurred only on clear days with no precipitation or road construction. Preliminary experiments by the author to find a balance in sensitivity to capture both linear and rotational motions from the vehicle confirmed intuition that the center of a vehicle was best. That is, placing the device too close to either wheel axle resulted in lower sensitivity to roughness at the opposite end of the vehicle. Therefore, the device captured data from the center seat of each vehicle. Securing the device flat onto the seat with adhesive tape provided a consistent coupling for all data collection sessions. The author used a level-finding app on the smartphone to assure that the device flatness was consistent among all installations. The installation pointed the longitudinal, or y-axis, of the smartphone integrated triaxial accelerometer in the direction of vehicle travel, the z-axis in the vertical direction, and the x-axis in the lateral direction of vehicle traversal. The author received approval to conduct experiments on the bus routes indicated in Fig. 2. The city granted access for experiments to any bus that used those routes. The route labels EM, SG, UG, MW, and WM denote the road segments shown from Essentia Hospital to the Mall, Sanford Hospital to the Ground Transportation Center, University Drive to the Ground Transportation Center, the Mall to Walmart, and Walmart to the Mall, respectively.

B. Data Format

The device software simultaneously sampled the output of each sensor at an average rate of 128 Hz to produce a table with samples of each variable in separate columns. One header contained the variable names and an additional header contained the route identifier, the unique vehicle identifier, and the date-time of the first sample. Each row thereafter contained one sample of each variable summarized in Table 1. In some cases, the agency used the same bus for multiple routes. Hence, the number of trips per bus ranged from 2 to 34 with an average

TABLE I
VARIABLES USED IN THE CALCULATIONS

Variables	Units	Description
L	meters	Longitudinal distance window
Time	millisecond	Time from start of traversal
Speed	meters per second	Ground speed of vehicle
Gx	g-force	Lateral linear acceleration
Gy	g-force	Longitudinal linear acceleration
Gz	g-force	Vertical linear acceleration
Rx	gradians per second	Angular velocity around the lateral axis (pitch rate)
Ry	gradians per second	Angular velocity around the longitudinal axis (roll rate)
Rz	gradians per second	Angular velocity around the vertical axis (yaw rate)

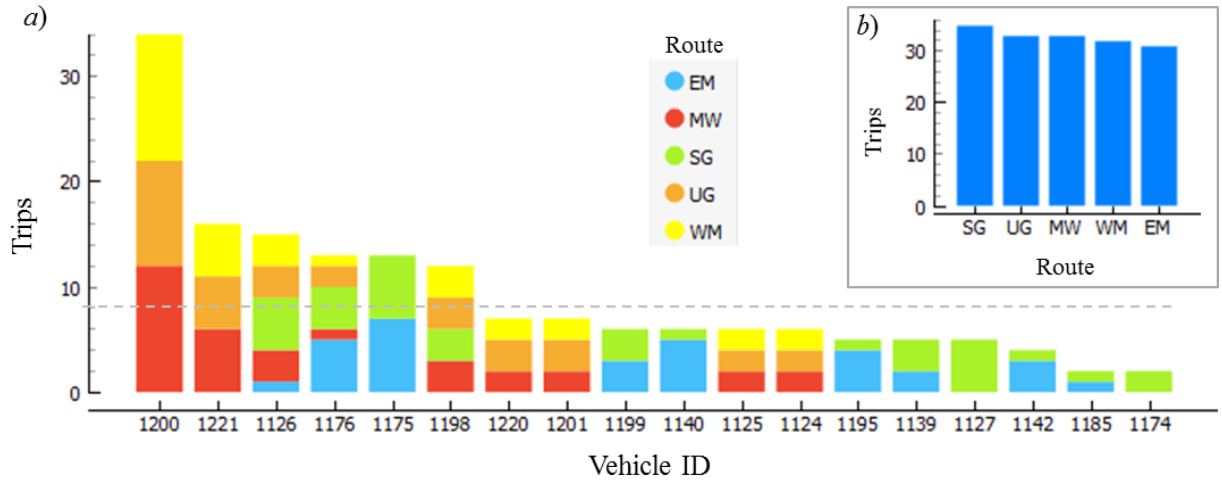

Fig. 3. Route map for data collection.

of 9 as summarized in Fig. 3a. Fig. 3b shows the number of measurements per route, which yielded a total of 164 files containing the signal samples summarized in Table 1. Considering the bus allocation constraints, the experiment design aimed for and achieved at least 30 trips per route to assure statistical significance [37]. Hence, the collected data represented a balanced sampling of the ride characteristics across each route.

C. Feature Extraction

Bridgelall (2014) developed the Road Impact Factor (RIF) transform to summarize vertical accelerations per unit of distance traveled [38]. The RIF-transform summarizes roughness in units of g-force experienced per meter of travel as

$$R_g^L = \sqrt{\frac{1}{L}\sum_{n=0}^{N-1} |g_n v_n|^2 \Delta t_n} \tag{3}$$

where g_n, v_n, and Δt_n are the g-force, speed, and sample interval, respectively, of the values sampled from the corresponding sensors. The distance L is the window size for each roughness index R_g^L computed along the traversal path.

The RIF-transform has several advantages over other direct methods of measuring ride quality. Those advantages are stability at non-uniform speeds, high data compression ratios, insensitivity to large sample interval variations, and the ability to localize roughness along a route by using a multiresolution spatial window [39]. The RIF-transform is stable at non-uniform speeds because it integrates the speed. That is, the RIF-index is zero when the speed is zero and increases monotonically as speed increases. The RIF-transform does not rely on a fixed sample interval for each sensor because the integration uses the instantaneous sample interval for each sample.

The data compression ratio γ of the RIF-transform is

$$\gamma = \frac{N_s}{N_R} = \frac{f_s T}{D/L} = L\frac{f_s T}{D} = L\frac{f_s}{\bar{v}} \tag{4}$$

where N_s and N_R are the number of raw data samples and RIF-indices, respectively. The means of the sample rate, traversal times, traversal distances, and traversal speed are f_s, T, D, and $\bar{v}$, respectively. For example, for a RIF window size of 10 meters, an average sample rate of 128 Hz, and an average traversal speed of 10 meters-per-second, the compression factor is 128. That is, with those parameters the transform will produce a roughness index after every 128 samples of the sensors. The tradeoff is spatial resolution in localizing roughness along the route, for example, when mapping the location of potholes and other roadway irregularities using a linear referencing system. To focus this research on evaluating the consistency and distinguishability of the CRI, this work does not elaborate on the localization capabilities inherited from the RIF-transform but instead points to previous work that did so [40].

D. Composite Roughness Index

Both surface irregularities and vehicle handling (accelerating, braking, turning) excite the vehicle suspension system, which dissipates energy as linear and rocking oscillations. Riders then experience one or more of the six force variations as roughness. From Newton's second law of motion, the *resultant* linear force acting on a mass m from combined lateral, longitudinal, and vertical accelerations is

$$F_\alpha = m\sqrt{g_x^2 + g_y^2 + g_z^2} \tag{5}$$

where g_x, g_y, and g_z are the accelerations measured along the lateral, longitudinal, and vertical spatial dimensions, respectively. Therefore, applying the RIF-transform to the individual acceleration components produces the corresponding RIF-indices R_x^L, R_y^L and R_z^L that summarize roughness along the lateral, longitudinal, and vertical directions, respectively. Hence, the Euclidean norm of the RIF-indices along each spatial dimension is the resultant RIF-index

$$R_\alpha^L = \sqrt{(R_x^L)^2 + \left(R_y^L\right)^2 + (R_z^L)^2} \tag{6}$$

which summarizes the resultant roughness experienced in the *linear* spatial dimensions per unit of distance L travelled.

As shown previously, the centrifugal force is directly proportional to the square of the rotation rate. Therefore,

applying the RIF-transform to each rotation rate component produces RIF-indices R_w^L, R_p^L and R_r^L that summarize roughness due to variations in angular velocity from yaw, pitch, and roll motions, respectively. Hence, the Euclidean norm of the RIF-indices from rotation rates about each spatial dimension is the resultant RIF-index

$$R_\theta^L = \sqrt{(R_w^L)^2 + \left(R_p^L\right)^2 + (R_r^L)^2} \tag{7}$$

From the centrifugal force equation, the square of the RIF-index of the resultant rotation rate is directly proportional to the resultant centrifugal force where

$$(R_\theta^L)^2 = \left(\sqrt{(R_w^L)^2 + \left(R_p^L\right)^2 + (R_r^L)^2}\right)^2 = (R_w^L)^2 + \left(R_p^L\right)^2 + (R_r^L)^2. \tag{8}$$

Consequently, the resultant roughness R_T^L experienced from both the linear and rotational motions is the Euclidean norm

$$R_T^L = \sqrt{(R_a^L)^2 + (R_\theta^L)^4} = \sqrt{(R_x^L)^2 + \left(R_y^L\right)^2 + (R_z^L)^2 + \left((R_w^L)^2 + \left(R_p^L\right)^2 + (R_r^L)^2\right)^2} \tag{9}$$

Interpreting the centrifugal forces in terms of g-forces require setting the linear and centrifugal forces equal as

$$ma = mr\omega^2 \leftrightarrow a = r\omega^2 \leftrightarrow g = \frac{r}{g}\omega^2 \tag{10}$$

where g is one unit of g-force or a = 9.8 m·s^{-2}. Hence, one can interpret the squared rotation rate as the g-force experienced at a radial distance of r = 9.8 meters such that

$$g = \omega^2. \tag{11}$$

Scaling the squared rotation rate by r/9.8 gives the g-force acting on a mass at any other radial distance r. For example, the centrifugal forces from head tossing due to rolling motion around the longitudinal axis is equivalent to the product of the squared rotation rate ω^2 measured and h/9.8 where h is the distance of one's head above the axis of rotation. This explains why roughness from rocking motion is more pronounced while standing in a vehicle versus sitting.

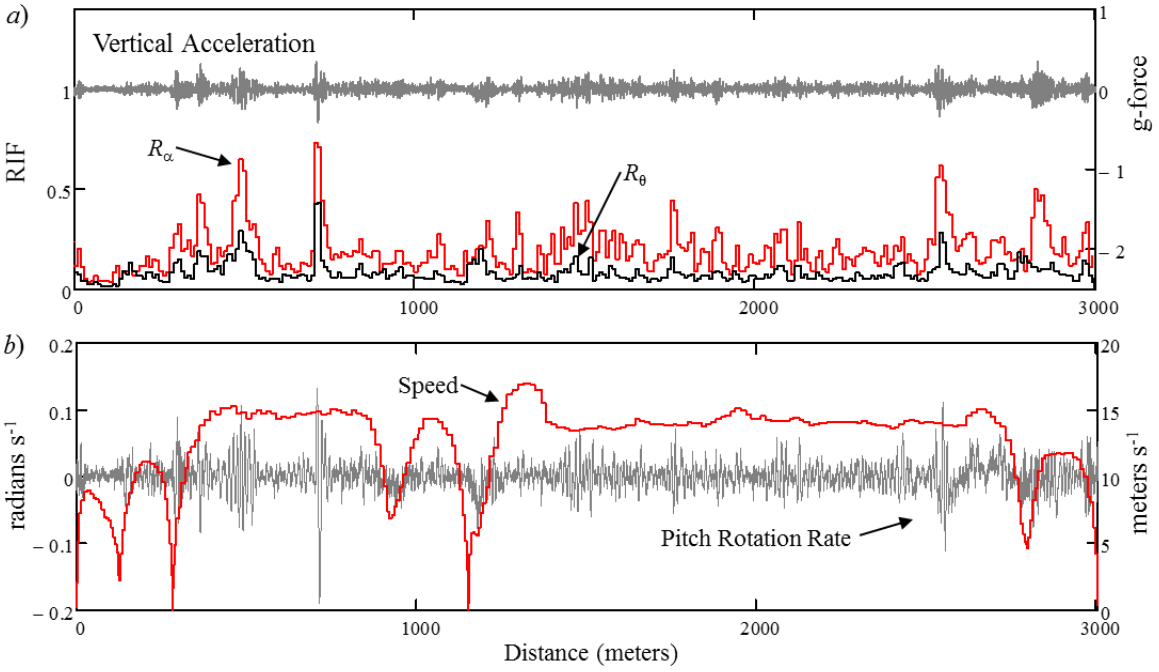

Fig. 4. Route map for data collection.

Fig. 4 illustrates examples of some of the raw and transformed signals. Fig. 4a plots the vertical acceleration (*Gz*) in units of g-force and Fig. 4b plots the pitch rotation rate (*Rx*) in units of radians-per-second. For this bus trip, the average magnitude of the resultant rotation rate was approximately half the average magnitude of the resultant linear acceleration. The stop-and-go bus ride is evident in the speed profile. The RIF-transform for these experiments used a window length of L = 10 meters to approximate the average bus length. The rationale is that if the vehicle traverses a single isolated road bump, then the RIF transform will summarize the roughness experienced after the full length of the vehicle moves past the road bump. The RIF-index for the overall traversal is the average of the RIF-indices from all distance windows along the route.

E. Feature Association

From Fig. 4, it is evident that positions of peak RIF-indices that characterize resultant roughness in the linear spatial dimensions tend to correspond to positions of peak resultant roughness from rotating motions. This suggests that are some associations among the six force components that produce the overall roughness experienced. It is important to verify that the observed associations are incidental because of the vehicle suspension design rather than a systematic dependency among force components that cause redundancy.

The Pearson correlation coefficient measures the amount of linear association between two variables ***X*** and ***Y*** based on their normalized covariance. The coefficient ranges from -1 to +1. A correlation coefficient of zero indicates that there is no linear correlation between the two variables. The Spearman

correlation coefficient is an alternative method that does not assess a linear relationship but instead assesses a statistical dependence between the *rankings* of two variables. Hence, the relationship between the variables can be linear or any monotonic non-linear function.

F. Consistency

A normal distribution of CRIs for the same route indicates a central tendency despite variations due to multiple factors. The major sources of variability include variations in speed, suspension system, operator handling, and wheel paths. The following optimization problem determined the best fit Gaussian curve to the distribution of CRIs for each route:

$$\begin{aligned} \underset{X_i}{\text{minimize}} \quad & e = \sum_{i=1}^{B} (H_i - G_i)^2 \\ \text{subject to} \quad & \alpha > 0, \sigma > 0, \text{and } N \geq B \geq 4 \\ \text{where} \quad & G_i = \frac{\alpha}{\sqrt{2\pi\sigma^2}} e^{-\frac{(X_i-\mu)^2}{2\sigma^2}} \\ & i = 1, 2, \ldots, B \end{aligned} \tag{12}$$

The histogram is a count H_i of values within interval X_i of bin i. The Gaussian function evaluated at the beginning of interval X_i yielded G_i where the amplitude α, mean μ, and variance σ^2 minimize the sum-of-squares error e. Subsequently, a Pearson's chi-squared test determined the goodness-of-fit based on the chi-squared statistic

$$\chi_k^2 = \sum_{i=1}^{B} \frac{(H_i - G_i)^2}{G_i} \tag{13}$$

The degrees-of-freedom (*DF*) associated with the chi-squared statistic is *k*, which is the number of histogram bins minus the three estimated parameters of α, μ, and σ. Hence, the *B* histogram bins must be at least four so that the *DF* can be at least unity, and the upper bound cannot exceed the number of samples *N*. The size of interval X_i is a function of the minimum CRI and the number of bins *B*. The probability *p* associated with the chi-squared statistic of the data is the area under the chi-squared distribution curve [41]. Hence, if the computed probability (p-value) is less than 0.05, then the test can reject the null hypothesis that the distribution follows the fitted Gaussian.

The margin-of-error (MOE) is a measure of the amount of clustering towards the mean. The MOE expresses the amount of variability in the measurement, thereby indicating the reliability of the mean. The MOE percentage for the distribution of a random variable within a (1-α)% confidence interval with significance α [41] is

$$MOE_{1-\alpha} = \pm \frac{\sigma \times t_{1-\alpha/2,DF}}{\mu\sqrt{N}} \tag{14}$$

where $t_{1-\alpha/2,df}$ is the *t*-score for a normalized cumulative t-distribution with *DF* degrees of freedom, μ is the mean, and σ is the standard deviation. The evaluation computed the MOE_{95}, which is the margin-of-error within a 95% confidence interval, to assess the trend as a function of *N* measurements.

G. Distinguishability

A standard t-test can determine if there is a statistically significant difference between the CRIs derived from only two routes at a time. A common strategy to apply the t-test to more than two groups at a time is to conduct individual tests for all possible pair-wise combinations of the groups. However, two crucial issues with such a strategy are the exponential increase in computational complexity with the number of groups, and the inflation of Type I error [37]. The later issue arises because the probability of a false positive increases with each additional t-test applied to the same dataset. Statisticians consequently developed the Analysis of Variance (ANOVA) method to generalize the t-test beyond two means [37]. The null hypothesis of the ANOVA test is that all groups are indistinct. The test rejects the null hypothesis if the p-value of the test statistic is less than the commonly set significance threshold of 0.05 for the p-value.

IV. RESULTS

The next subsections parallel the methods section to evaluate the feature association, the consistency of the CRIs, and the distinguishability of the CRIs among the different routes.

A. Feature Association

Fig. 5 plots both the Pearson and Spearman coefficients for all

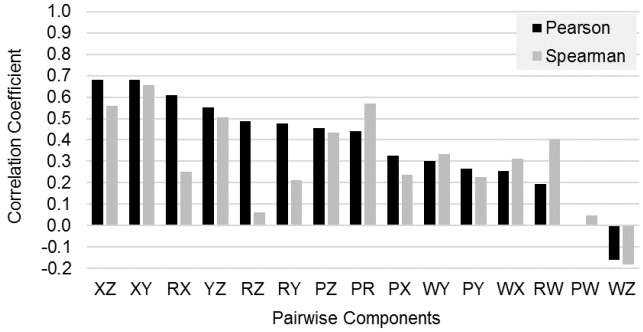

Fig. 5. Cross-correlations for the pairwise components across all traversals.

pairwise combination of the six RIF-index components of CRIs derived from all routes. The letter pairs indicate correlations between the average RIF-index components from lateral (X), longitudinal (Y), vertical (Z), pitch (P), roll (R), or yaw (W) motions. All values are above zero but significantly smaller than 1.0. This result indicates that, although there are some interactions among the six movement directions based on correlation values greater than 0.6, there are no overall dependencies because most correlation values are lower than 0.5. Therefore, roughness from each of the six motion components contribute differently to the overall ride roughness. This result concludes that there are no redundancies among the six roughness components.

All values are positive except WZ, which indicates that high yaw rates tend to correspond to low vertical accelerations, and vice versa. This finding is intuitive because the vehicle tends to move more slowly when turning, thus generating lower vertical accelerations from road roughness.

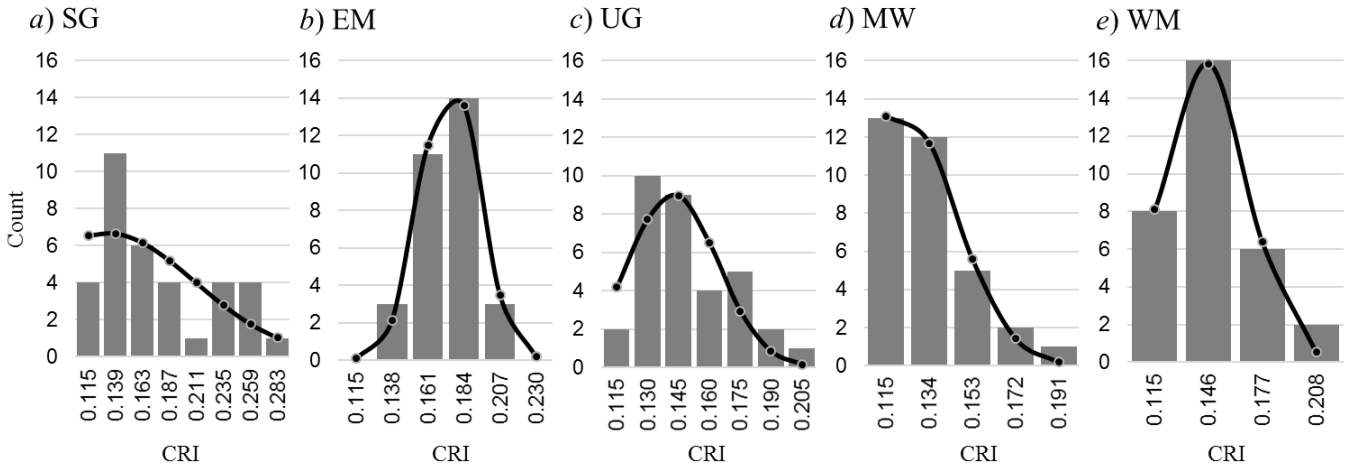

Fig. 6. CRI distribution and best fitted Gaussian curve for each route.

B. *Consistency*

The bar charts of Fig. 6 show the distributions of CRIs derived for each route. The curves overlaying the bars are the best-fit Gaussian functions from the optimization procedure defined earlier. Table 2 summarizes the key statistics for each distribution. For interpretability, a skew equaling zero means that the distribution is perfectly symmetric about the mean [37]. The non-zero skew indicates the amount of deviation from the normal distribution. Variability due to additional factors such as suspension system and speed differences among the vehicles traversing the same route contributed to the deviation from a Gaussian curve.

Fig. 7 shows the variability in CRI derived from each vehicle traversing the same route. The first three digits of the Vehicle ID encode the vehicle manufacturer and model year and the next four digits are the bus numbers. Variations in the suspension system behavior include variations in loading and differences in tire pressure. Fig. 8 shows the variability in average speed by vehicle for each route. As observed, traversals of route SG had the largest variation of CRI, which its largest speed variation by vehicle partially explained.

Despite deviations from a standard normal distribution, the p-values from the chi-squared statistic were all greater than 0.05, meaning that the tests could not reject the null hypothesis that the CRIs distribute normally. The implication is that differences in suspension system response and speed variability did not significantly distort the distribution of the CRIs from a normal distribution.

The kurtosis of a normally distributed variable is 3, with lower values indicating fewer extreme values than those of a normal distribution [37]. Hence, the relatively low kurtosis values for the distributions of the CRIs suggest that the CRIs had a low propensity to contain outliers.

Fig. 9 plots the MOE_{95} as a function of the number of traversals, N. The declining trend indicates that the consistency of CRIs will increase with additional measurements for each route. As indicated in the inset, the relatively high R^2 value for the fitted curve provides a high confidence that the declining

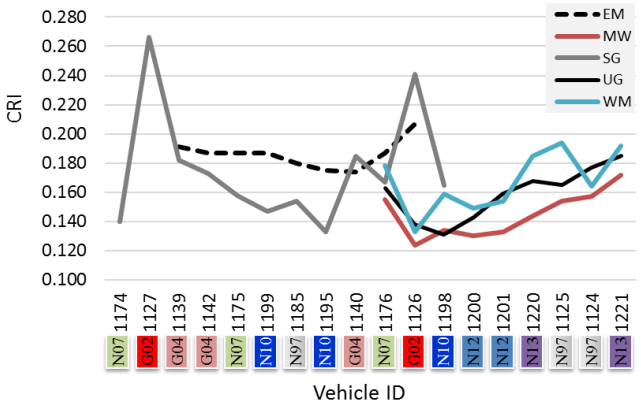

Fig. 7. Mean CRI by vehicle and route.

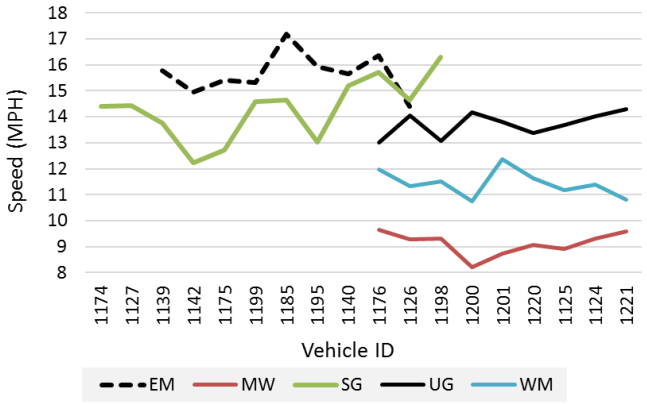

Fig. 8. Mean speed by vehicle and route.

TABLE II
SUMMARY OF DISTRIBUTION STATISTICS

Parameter	SG	EM	UG	MW	WM
N	35	31	33	33	32
CRI Mean	0.188	0.184	0.156	0.143	0.163
CRI STD	0.047	0.017	0.022	0.020	0.022
CRI Min	0.128	0.147	0.115	0.115	0.130
CRI Max	0.294	0.212	0.219	0.208	0.211
Skew	0.74	-0.30	0.76	1.36	0.78
Kurtosis	-0.74	-0.78	0.58	1.93	-0.29
χ^2 statistic	9.61	0.76	10.60	3.51	4.18
DF	7	7	11	9	5
p-value	0.212	0.998	0.477	0.941	0.523
Reject Normality	No	No	No	No	No

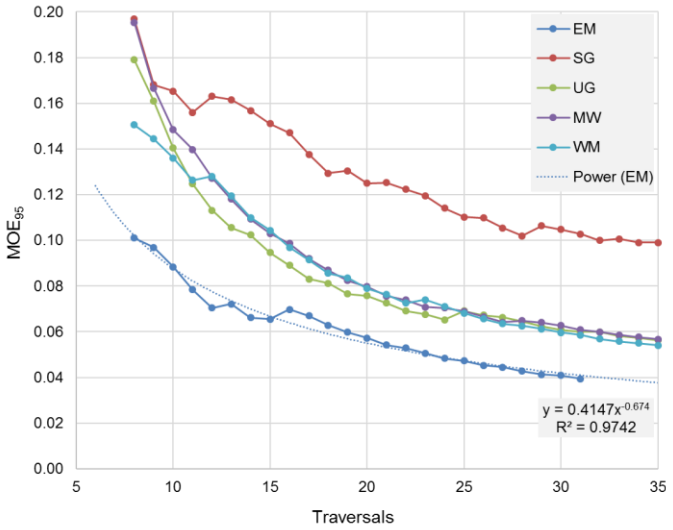

Fig. 9. MOE trends with sample size for each route.

trend will continue as a negative power curve.

C. Distinguishability

Fig. 10 compares the best fitted Gaussian curve to the distributions of the CRIs for each route. Visually, the means μ and the standard deviations σ appear to be distinguishable. The

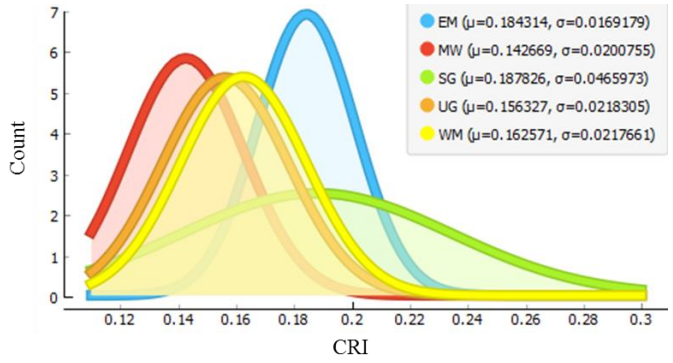

Fig. 10. Comparison of best fitted Gaussian curve for each route

ANOVA tests confirm the distinguishability of CRIs based on p-values that are much smaller than 0.05 as summarized in Table 3. Applying the ANOVA tests to each of the six roughness index components also show that those measurements are distinguishable among the routes. The last two columns are the ANOVA and p-values, respectively. Alternate rows are the mean values and the standard deviations for each roughness component. The only rejection of the null hypothesis is for the RIF-indices of the pitch rotation rates. However, the test cannot reject the null hypothesis at a slightly higher significance threshold of 0.08 instead of 0.05. This borderline distinguishability of pitch rotation rates suggests that changes in vehicle pitch due to acceleration and deceleration patterns may be similar across routes.

V. Discussion

A sudden drop in the altitude of an aircraft because of turbulence produces a vertical force that pushes a passenger away from the seat. The rapid acceleration or abrupt braking of a bus produces longitudinal forces that push the body towards the rear or front of the seat, respectively. Speeding around a curve produces a centrifugal force that pushes the body towards the side of the vehicle. These familiar manifestations of roughness are due to both linear accelerations along the three spatial axes, and rotations around those axes. The CRI encapsulates the overall roughness from force changes felt from those six independent movements in the three spatial dimensions.

The measures of association among the six RIF-index components showed that there was no significant coupling that caused redundancies in the CRI. The tests for normality of the distribution of CRIs showed that while there were some deviations from a perfect Gaussian curve because of explained variances from vehicle suspension system and speed, the distributions of CRIs did not deviate significantly from the normal distribution. The consistent decrease in MOE_{95} with each additional measurement suggested that, despite variations from the explained external factors, the CRIs were consistent for each of the routes characterized. The ANOVA tests showed that the CRIs, including all their roughness components, were distinguishable among the five routes characterized.

A limitation of the approach is that external factors that introduce variability among the measurements reduce consistency and precision. These experiments did not attempt to control variability due to vehicle type, vehicle speed profile, vehicle loading, tire pressure, wheel path, driver behavior, and possible environmental factors such as temperature and wind. However, using the identical smartphone model, software, device mount, and location within the vehicle for all experiments helped to reduce measurement variations from those factors.

Even with the uncontrolled variations, the experiments showed that consistency improved steadily with each additional measurement across the same traversal path. Therefore, applications that use in-situ sensors or crowdsensing are well-suited to the approach. Although the experiments used a single point source to measure force changes and rotations, replications of the approach can average the RIF-indices for each component from multiple point sources. The availability

TABLE III
DISTINGUISHABILITY TESTS BY ANOVA

	EM	SG	UG	MW	WM	A-val	p-val
R_x^L	0.057	0.061	0.050	0.054	0.054	5.1	0.001
	0.009	0.018	0.008	0.006	0.009		
R_y^L	0.055	0.056	0.051	0.053	0.057	2.2	0.074
	0.010	0.013	0.008	0.006	0.008		
R_z^L	0.166	0.165	0.139	0.120	0.142	19.0	0.000
	0.016	0.039	0.021	0.020	0.021		
R_p^L	0.056	0.049	0.047	0.042	0.050	13.3	0.000
	0.005	0.010	0.008	0.006	0.008		
R_r^L	0.061	0.107	0.060	0.058	0.065	6.3	0.000
	0.035	0.094	0.027	0.014	0.018		
R_w^L	0.022	0.023	0.020	0.036	0.031	111.1	0.000
	0.003	0.005	0.003	0.003	0.004		
R_α^L	0.184	0.185	0.156	0.142	0.162	15.0	0.000
	0.017	0.043	0.022	0.020	0.022		
R_θ^L	0.006	0.021	0.005	0.004	0.005	8.2	0.000
	0.009	0.029	0.004	0.002	0.003		
R_T^L	0.184	0.187	0.156	0.143	0.162	15.0	0.000
	0.017	0.047	0.022	0.020	0.022		

of smartphones that integrate all the required sensors and functionality reduces the cost and burden of scaling such data collection sessions. As connected vehicles evolve to include all the required in-situ sensors, the reduced variability and large data volume will result in an ever-increasing consistency and distinguishability of the CRIs.

VI. Conclusion

Despite the focus on characterizing ride quality from roadways, there are many other important applications of roughness characterization that the existing international roughness index (IRI) standard cannot address. Consequently, this work proposed a composite roughness index (CRI) to characterize roughness from force changes resulting from linear accelerations along the three spatial dimensions, and rotations around their corresponding axes. The methods to define and evaluate the CRI demonstrated that, when used to characterize ride quality, the CRI is both statistically consistent and distinguishable among routes. With each additional CRI measured, the consistency improves with the ever-decreasing margin of error of the mean. The ANOVA tests established that the CRIs are distinguishable among traversal paths.

The use of smartphones that contain all the required sensors and software increases the convenience and affordability of replicating and scaling the method to assess ride quality for many other applications not yet discussed or even conceived. Researchers can follow the procedures in this manuscript to replicate the results or scale the experiments to other modes of transport. Prior to the widespread availability of connected vehicles, agencies can use smartphones aboard accessible vehicles such as utility, law enforcement, emergency response, or public transit vehicles to evaluate the relative ride quality of roadways by comparing their CRI distributions. In future research, the authors plan to determine a suitable partition of the CRI range that corresponds to psychological ratings of ride comfort.

Acknowledgement

The authors are grateful to the Transit Administrators of the City of Fargo for facilitating and approving the data collection.

References

[1] T. D. Gillespie, M. W. Sayers and C. A. V. Queiroz, "The International Road Roughness Experiment: Establishing Correlation and Calibration Standard for Measurement," The World Bank, Washington, D.C., 1986.

[2] P. Múčka, "International Roughness Index specifications around the world," *Road Materials and Pavement Design*, vol. 18, no. 4, pp. 929-965, 2017.

[3] G. Loprencipe and P. Zoccali, "Use of generated artificial road profiles in road roughness evaluation," *Journal of Modern Transportation*, vol. 25, no. 1, pp. 24-33, 2017.

[4] M. Coni, F. Maltinti, F. Pinna, N. Rassu, C. Garau, B. Barabino and G. Maternini, "On-Board Comfort of Different Age Passengers and Bus-Lane Characteristics," in *Computational Science and Its Applications – ICCSA 2020. ICCSA 2020. Lecture Notes in Computer Science*, Cham, 2020.

[5] M. Elbanhawi, M. Simic and R. Jazar, "In the Passenger Seat: Investigating Ride Comfort Measures in Autonomous Cars," *IEEE Intelligent Transportation Systems Magazine*, vol. 7, no. 3, pp. 4-17, 2015.

[6] M. Pierucci and M. Frederick, "Ride quality and noise in high speed elevators," *Journal of the Acoustical Society of America*, vol. 123, no. 5, pp. 3247-3247, 2008.

[7] F. Ripamonti and A. Chiarabaglio, "A smart solution for improving ride comfort in high-speed railway vehicles," *Journal of Vibration and Control*, vol. 25, no. 13, pp. 1958-1973, 2019.

[8] A. a. Wåhlberg, "Short-term effects of training in economical driving; passenger comfort and driver acceleration behavior," *International Journal of Industrial Ergonomics*, vol. 36, no. 2, pp. 151-163, 2006.

[9] T. Partridge, L. Gherman, D. Morris, R. Light, A. Leslie, D. Sharkey, D. McNally and J. Crowe, "Smartphone monitoring of in-ambulance vibration and noise.," *Proceedings of the Institution of Mechanical Engineers, Part H: Journal of Engineering in Medicine*, vol. 235, no. 4, pp. 428-436, 2021.

[10] S. Wang and S. Zhu, "Impact source localization and vibration intensity prediction on construction sites," *Measurement*, vol. 175, p. 109148, 2021.

[11] I. Fernando, J. Fei, R. Stanley and H. Enshaei, "Measurement and evaluation of the effect of vibration on fruits in transit—review," *Packaging Technology and Science*, vol. 31, no. 11, pp. 723-738, 2018.

[12] J. Duvall, E. Sinagra, R. Cooper and J. Pearlman, "Proposed pedestrian pathway roughness thresholds to ensure safety and comfort for wheelchair users.," *Assistive Technology*, vol. 28, no. 4, pp. 209-215, 2016.

[13] J. M. W. Brownjohn and T. N. Fu, "Vibration excitation and control of a pedestrian walkway by individuals and crowds," *Shock and Vibration*, vol. 12, no. 5, pp. 333-347, 2005.

[14] L. Eboli, G. Mazzulla and G. Pungillo, "Combining speed and acceleration to define car users' safe or unsafe driving behaviour," *Transportation Research Part C-emerging Technologies*, vol. 68, no. 68, pp. 113-125, 2016.

[15] S. Arumugam and R. Bhargavi, "A survey on driving behavior analysis in usage based insurance using big data," *Journal of Big Data*, vol. 6, no. 1, pp. 1-21, 2019.

[16] P. Múčka, "Current approaches to quantify the longitudinal road roughness," *International Journal of Pavement Engineering*, vol. 17, no. 8, pp. 659-679, 2016.

[17] T. D. Gillespie and S. M. Karamihas, "Simplified models for truck dynamic response to road inputs," *International Journal of Heavy Vehicle Systems*, vol. 7, no. 1, pp. 52-63, 2000.

[18] T. Nguyen, B. Lechner, Y. D. Wong and J. Y. Tan, "Bus Ride Index – a refined approach to evaluating road surface irregularities," *Road Materials and Pavement Design*, vol. 22, no. 2, pp. 423-443, 2021.

[19] S. M. Piryonesi and T. E. El-Diraby, "Examining the relationship between two road performance indicators: Pavement condition index and international roughness index," *Transportation geotechnics*, vol. 26, p. 100441, 2021.

[20] A. Alhasan, D. J. White and K. D. Brabanterb, "Continuous wavelet analysis of pavement profiles," *Automation in Construction*, vol. 63, pp. 134-143, 2016.

[21] P. Múčka, "Vibration Dose Value in Passenger Car and Road Roughness," *Journal of Transportation Engineering, Part B: Pavements*, vol. 146, no. 4, p. 4020064, 2020.

[22] E. OBrien, Y. Li and A. González, "Bridge roughness index as an indicator of bridge dynamic amplification," *Computers & Structures*, vol. 84, no. 12, pp. 759-769, 2006.

[23] ISO 2631-5:2018, "Mechanical vibration and shock — Evaluation of human exposure to whole-body vibration — Part 5: Method for evaluation of vibration containing multiple shocks," International Organization for Standardization (ISO), Geneva, Switzerland, 2018.

[24] EN 12299, "Railway applications - Ride comfort for passengers - Measurement and evaluation," European Committee for Standardization (CEN), Brussels, 2009.

[25] G. Maternini and M. Cadei, "A comfort scale for standing bus passengers in relation to certain road characteristics," *Transportation Letters: The International Journal of Transportation Research*, vol. 6, no. 3, pp. 136-141, 2014.

[26] B. Barabino, M. Coni, A. Olivo, G. Pungillo and N. Rassu, "Standing Passenger Comfort: A New Scale for Evaluating the Real-Time Driving Style of Bus Transit Services," *IEEE Transactions on Intelligent Transportation Systems*, vol. 20, no. 12, pp. 4665-4678, 2019.

[27] G. Loprencipe, F. G. V. d. A. Filho, R. H. d. Oliveira and S. Bruno, "Validation of a Low-Cost Pavement Monitoring Inertial-Based System for Urban Road Networks.," *Sensors*, vol. 21, no. 9, p. 3127, 2021.

[28] N. S. P. Peraka and K. P. Biligiri, "Pavement asset management systems and technologies: A review," *Automation in Construction*, vol. 119, p. 103336, 2020.

[29] S. Sattar, S. Li and M. A. Chapman, "Road Surface Monitoring Using Smartphone Sensors: A Review.," *Sensors*, vol. 18, no. 11, p. 3845, 2018.

[30] X. Yang, L. Hu, H. U. Ahmed, R. Bridgelall and Y. Huang, "Calibration of smartphone sensors to evaluate the ride quality of paved and unpaved roads," *International Journal of Pavement Engineering*, pp. 1-11, 2020.

[31] Y. Ma, Z. Zhang, S. Chen, Y. Yu and K. Tang, "A Comparative Study of Aggressive Driving Behavior Recognition Algorithms Based on Vehicle Motion Data," *IEEE Access*, vol. 7, pp. 8028-8038, 2019.

[32] J. R. Medina, R. Salim, B. S. Underwood and K. Kaloush, "Experimental Study for Crowdsourced Ride Quality Index Estimation Using Smartphones," *Journal of Transportation Engineering, Part B: Pavements*, vol. 146, no. 4, p. 4020070, 2020.

[33] H. Zhao, L.-L. Guo and X.-Y. Zeng, "Evaluation of Bus Vibration Comfort Based on Passenger Crowdsourcing Mode," *Mathematical Problems in Engineering*, vol. 2016, pp. 1-10, 2016.

[34] T.-Y. Chuang, N.-H. Perng and J.-Y. Han, "Pavement performance monitoring and anomaly recognition based on crowdsourcing spatiotemporal data," *Automation in Construction*, vol. 106, p. 102882, 2019.

[35] T. Nguyen, B. Lechner and Y. D. Wong, "Response-based methods to measure road surface irregularity: a state-of-the-art review," *European Transport Research Review*, vol. 11, no. 1, pp. 1-18, 2019.

[36] H. D. Young and R. A. Freedman, University Physics Volume 1, 15th ed., London: Pearson, 2019, p. 752.

[37] S. Boslaugh, Statistics in a nutshell: A desktop quick reference, Sebastopol, California: O'Reilly Media, Inc., 2013.

[38] R. Bridgelall, "Connected Vehicle Approach for Pavement Roughness Evaluation," *Journal of Infrastructure Systems*, vol. 20, no. 1, pp. 04013001 (1-6), 23 April 2014.

[39] R. Bridgelall, M. T. Rahman, D. Tolliver and J. F. Daleiden, "Wavelength sensitivity of roughness measurements using connected vehicles," *International Journal of Pavement Engineering*, vol. Online, pp. 1-7, 18 April 2017.

[40] R. Bridgelall and D. Tolliver, "Accuracy enhancement of roadway anomaly localization using connected vehicles," *International Journal of Pavement Engineering*, vol. 19, no. 1, pp. 75-81, 2018.

[41] A. Agresti, Statistical Methods for the Social Sciences, 5th ed., Boston, Massachusetts: Pearson, 2018, p. 608.

Dr. Raj Bridgelall (M'91-SM'02) Bridgelall received a Ph.D. degree in transportation and logistics at the North Dakota State University (NDSU), Fargo in 2015. He is a program director of the Intelligent Transportation Systems Center, and an assistant professor with the Department of Transportation, Logistics, and Finance, NDSU.